Optical cavity squeezing of multiwave mixing via dark states

Yiqi Zhang, Xun Zhang, Haixia Chen, Peiying Li, Mengqin Gao, Zihai Jiang, and Yanpeng Zhang*

Key Laboratory for Physical Electronics and Devices of the Ministry of Education & Shaanxi Key Laboratory of Information Photonic Technique, Xi'an Jiaotong University, Xi'an 710049, China
**Corresponding author: ypzhang@mail.xjtu.edu.cn*

Received August 4, 2014; revised September 11, 2014; accepted September 17, 2014;
posted September 18, 2014 (Doc. ID 217166); published October 22, 2014

We theoretically demonstrate the influence of dark states on single-mode and two-mode optical squeezing in a four-level atomic–cavity coupling system through fifth- and third-order cascade nonlinearity. We first show the cone emissions of self-diffraction and phase-conjugate spontaneous parametric (SP) four-wave mixing processes. Then, we inject a coherent or Einstein–Podolsky–Rosen field into the SP-MWM channels to investigate the corresponding squeezing. The investigations have potential applications in quantum information processing. © 2014 Optical Society of America

OCIS codes: (270.6570) Squeezed states; (190.4223) Nonlinear wave mixing; (190.4380) Nonlinear optics, four-wave mixing; (190.4410) Nonlinear optics, parametric processes.
http://dx.doi.org/10.1364/JOSAB.31.002792

1. INTRODUCTION

The squeezed state of light is a typical nonclassical field, which can be generated by nonlinear optical processes such as multiwave mixing (MWM) [1] or parametric interaction [2]. Due to its intriguing quantum features, optical squeezing attracts many researchers' interest. To the best of our knowledge, entangled images from four-wave mixing (FWM) can be implemented by using two-mode quadrature squeezing in free space [3], and the tunable delay of Einstein–Podolsky–Rosen (EPR) entanglement can be achieved by FWM squeezing [4]. The degree of squeezing between amplitude and phase quadratures of EPR beams can be enhanced if there is injection [5]. In experiment, quantum interference phenomena in the phase-sensitive optical parametric amplification (OPA) system inside an optical cavity with an injected squeezed vacuum state was demonstrated [6], and quantum fluctuation spectra in two coupled optical cavities with an injected squeezed vacuum state was also observed [7].

In addition, as a result of atomic coherence, electromagnetically induced transparency (EIT) [8,9] and dressed MWM [10,11] also attract a lot of attention. Especially the enhancement and suppression [12], that can be used to control the probe and MWM signals, are quite involved. It is worth mentioning that the enhancement and suppression can be multiparametrically controlled, including the frequency detunings and powers. Recently, our group has observed Autler–Towns (AT) splitting and dressed FWM [13,14] in multilevel atomic vapors. Also, we have demonstrated the existence of the cascade nonlinear process by injecting classical FWM or six-wave mixing (SWM) to the parametric FWM or SWM channels [15].

In this paper, we apply the suppression and enhancement theory to the spontaneous parametric (SP) MWM process to study single-mode and two-mode squeezing in detail. We successfully manipulate quantum squeezing through dark states. The paper is organized as follows: in Section 2, we briefly introduce the basic theory, and in Sections 3 and 4, we study single-mode and two-mode squeezing in detail. In Section 5, we conclude the paper.

2. SP-MWM PROCESSES AND SPATIAL PROPERTIES

A. SP-MWM Processes

An inverted-Y-type energy level system as shown in Fig. 1 is constructed by four energy levels $|0\rangle$, $|1\rangle$, $|2\rangle$, and $|3\rangle$. Three laser beams $\mathbf{k}_1$, $\mathbf{k}_2$, and $\mathbf{k}_3$ drive $|0\rangle\leftrightarrow|1\rangle$, $|1\rangle\leftrightarrow|2\rangle$, and $|1\rangle\leftrightarrow|3\rangle$, respectively. In this energy level system, we discuss three kinds of subsystems in which three kinds of optical SP-MWM processes are generated. First, a Λ-type subsystem $|0\rangle-|1\rangle-|3\rangle$ can generate two SP-FWM processes $\mathbf{k}_{F1}$ and $\mathbf{k}_{F3}$ satisfying phase-matching conditions $\mathbf{k}_{F1}=\mathbf{k}_1-\mathbf{k}_{F3}+\mathbf{k}_3$ and $\mathbf{k}_{F3}=\mathbf{k}_3-\mathbf{k}_{F1}+\mathbf{k}_1$, respectively. Here, $\mathbf{k}_2$ serves as a dressing field. Second, a ladder-type subsystem $|0\rangle-|1\rangle-|2\rangle$ can generate another two SP-FWM processes $\mathbf{k}_{F1'}$ and $\mathbf{k}_{F2}$ satisfying $\mathbf{k}_{F1'}=\mathbf{k}_1-\mathbf{k}_{F2}+\mathbf{k}_2$ and $\mathbf{k}_{F2}=\mathbf{k}_2-\mathbf{k}_{F4}+\mathbf{k}_1$, respectively. Now, $\mathbf{k}_3$ is the dressing field. Third, three SP-SWM processes $\mathbf{k}_{S1}$, $\mathbf{k}_{S2}$, and $\mathbf{k}_{S3}$, respectively, satisfying $\mathbf{k}_{S1}=\mathbf{k}_1+\mathbf{k}_2-\mathbf{k}_{S2}+\mathbf{k}_3-\mathbf{k}_{S3}$, $\mathbf{k}_{S2}=\mathbf{k}_2+\mathbf{k}_1-\mathbf{k}_{S1}+\mathbf{k}_3-\mathbf{k}_{S3}$, and $\mathbf{k}_{S3}=\mathbf{k}_3+\mathbf{k}_1-\mathbf{k}_{S1}+\mathbf{k}_2-\mathbf{k}_{S2}$ can be generated in this inverted-Y-type energy level system. Here, we would like to name the two SP-FWM processes self-diffraction and phase-conjugate FWM processes, which generate $\mathbf{k}_{F1}$ & $\mathbf{k}_{F3}$ and $\mathbf{k}_{F1'}$ & $\mathbf{k}_{F2}$, respectively.

B. Spatial Properties of SP-MWM Processes

1. Self-Diffraction SP-FWM Cone Emission

Under undepleted pump approximation, we can get the coupling equations for the two space-dependent correlated photons [$\hat{a}_{F1}(z)$ & $\hat{a}_{F3}(z)$ and $\hat{a}_{F1'}(z)$ & $\hat{a}_{F2}(z)$] [16]

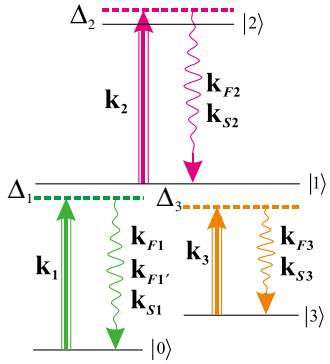

Fig. 1. Scheme of an inverted-Y-type energy level system.

$$\frac{d\hat{a}_{F1,F1'}(z)}{dz} = (\kappa_{F1,F1'} + i\kappa'_{F1,F1'}) \times \exp[i(\Delta k z + \varphi_1 + \varphi_{3,2})]\hat{a}^{+}_{F3,F2}(z), \quad (1a)$$

$$\frac{d\hat{a}_{F3,F2}(z)}{dz} = (\kappa_{F3,F2} + i\kappa'_{F3,F2}) \times \exp[i(\Delta k z + \varphi_1 + \varphi_{3,2})]\hat{a}^{+}_{F1,F1'}(z), \quad (1b)$$

where

$$\kappa_{F1,F1'} = \mathrm{Re}[(-i\varpi_{F1,F1'}/2c)\chi^{(3)}_{F1,F1'}E_1E_{3,2}]$$

and

$$\kappa'_{F1,F1'} = \mathrm{Im}[(-i\varpi_{F1,F1'}/2c)\chi^{(3)}_{F1,F1'}E_1E_{3,2}]$$

are the nonlinear coefficients for $\mathbf{k}_{F1,F1'}$,

$$\kappa_{F3,F2} = \mathrm{Re}[(-i\varpi_{F3,F2}/2c)\chi^{(3)}_{F3,F2}E_1E_{3,2}]$$

and

$$\kappa'_{F3,F2} = \mathrm{Im}[(-i\varpi_{F3,F2}/2c)\chi^{(3)}_{F3,F2}E_1E_{3,2}]$$

for $\mathbf{k}_{F3,F2}$. $\phi_{1,2,3}$ is the phase of $\mathbf{k}_{1,2,3}$, z is the propagation distance of the waves, and $\Delta k = \Delta k_z$ ($\Delta k_x = \Delta k_y = 0$) is the phase mismatching. $\varpi_{F1} = \Omega_{10} - \Delta_3$, $\varpi_{F3} = \Omega_{13} - \Delta_1$, $\varpi_{F1'} = \Omega_{10} - \Delta_2$, and $\varpi_{F2} = \Omega_{21} - \Delta_1$ are the central frequencies of generated photons. Furthermore, the third-order nonlinear susceptibility $\chi^{(3)}$ in the nonlinear coefficients can be obtained from the corresponding density matrix elements as $\chi^{(3)}_{F1,F3} = (N\mu_{10}^2\mu_{13}^2\rho^{(3)}_{F1,F3})/(\varepsilon_0\hbar^3G_1G_3G_{F3,F1})$ and $\chi^{(3)}_{F1',F2} = (N\mu_{10}^2\mu_{21}^2\rho^{(3)}_{F1',F2})/(\varepsilon_0\hbar^3G_1G_2G_{F2,F1'})$, where N is the density of atoms, ε_0 is permittivity, μ_{ij} is the transition dipole moment between the levels $|i\rangle$ and $|j\rangle$, and $G_i = \mu_{ij}E_i/\hbar$ is the Rabi frequency for the laser $\mathbf{k}_i$.

For computation convenience, we assume $\kappa_{F1,F1'} = \kappa_{F3,F2}$, $\kappa_{F1,F1'} \gg \kappa'_{F1,F1'}$, and $\kappa_{F3,F2} \gg \kappa'_{F3,F2}$ [17]. Therefore, we obtain

$$\hat{a}_{F1,F1'}(z) = e^{i\frac{\Delta k}{2}z}\left(C - i\frac{\Delta k}{2K}S\right)\hat{a}_{F1,F1'}(0) + e^{i(\frac{\Delta k}{2}z+2\phi)}\left(\frac{g}{K}S\right)\hat{a}^{+}_{F3,F2}(0), \quad (2a)$$

$$\hat{a}_{F3,F2}(z) = e^{i(\frac{\Delta k}{2}z+2\phi)}\left(\frac{g}{K}S\right)\hat{a}^{+}_{F1,F1'}(0) + e^{i\frac{\Delta k}{2}z}\left(C - i\frac{\Delta k}{2K}S\right)\hat{a}_{F3,F2}(0), \quad (2b)$$

where $C = \cosh(Kz)$, $S = \sinh(Kz)$, $K = \sqrt{\kappa^2 - (\Delta k/2)^2}$ in case $\kappa^2 > (\Delta k/2)^2$, and $C = \cos(Kz)$, $S = \sin(Kz)$, $K = \sqrt{(\Delta k/2)^2 - \kappa^2}$ in case $\kappa^2 \le (\Delta k/2)^2$, $\phi = \phi_1 + \phi_{2,3} - \phi_{F1,F1'} - \phi_{F3,F2}$ is the relative phase among $\mathbf{k}_1$, $\mathbf{k}_{3,2}$, and the seeding beams at $\mathbf{k}_{F1,F1'}$ and $\mathbf{k}_{F3,F2}$ channels.

When there is no seeding in this SP-FWM process, the output states are two-mode squeezed vacuum states [18–21]. Via the pathway $\rho^{(0)}_{00} \xrightarrow{\omega_1} \rho^{(1)}_{10} \xrightarrow{-\omega_{F3}} \rho^{(2)}_{30} \xrightarrow{\omega_3} \rho^{(3)}_{10F1}$ and considering the dressing effect of $\mathbf{k}_2$, the density matrix element for $\mathbf{k}_{F1}$ is

$$\rho^{(3)}_{F1} = \frac{-iG_1G^*_{F3}G_3}{(d_{10} + |G_2|^2/d_{20})d_{03+}(d_{13} + |G_2|^2/d'_{20})}, \quad (3)$$

where Γ_{ij} is the transverse decay rate between levels $|i\rangle$ and $|j\rangle$, $d_{10} = \Gamma_{10} + i\Delta_1$, $d_{20} = \Gamma_{20} + i(\Delta_1 + \Delta_2)$, $d_{03+} = \Gamma_{03} + i\delta$, $d_{13} = \Gamma_{13} + i(\Delta_1 + \delta)$, and $d'_{20} = \Gamma_{20} + i(\Delta_3 + \delta + \Delta_2)$. The detuning is defined as $\Delta_i = \Omega_i - \omega_i$ with Ω_i being the resonant frequency between the levels that E_i connects, and $\delta = \omega_F - \varpi_F$. Similarly, we can obtain the density matrix element via $\rho^{(0)}_{00} - \omega_{F1} \to \rho^{(1)}_{01}\omega_3 \to \rho^{(2)}_{03}\omega_1 \to \rho^{(3)}_{13F3}$ for $\mathbf{k}_{F3}$,

$$\rho^{(3)}_{F3} = \frac{-iG^*_{F1}G_3G_1}{(d_{01} + |G_2|^2/d_{02})d_{03-}(d_{13'} + |G_2|^2/d_{23})}, \quad (4)$$

where $d_{01} = \Gamma_{01} - i(\Delta_3 + \delta)$, $d_{02} = \Gamma_{02} - i(\Delta_3 + \delta + \Delta_2)$, $d_{03-} = \Gamma_{03} - i\delta$, $d'_{13} = \Gamma_{13} + i(\Delta_1 - \delta)$, and $d_{23} = \Gamma_{23} + i(\Delta_1 + \Delta_2 - \delta)$.

The geometric distribution of $\mathbf{k}_1$, $\mathbf{k}_3$, $\mathbf{k}_{F1}$, and $\mathbf{k}_{F3}$ is shown in Fig. 2(a). According to the geometric relation, we obtain the phase mismatching conditions

$$\Delta k_{F1} = k_1 + k_3 - k_{F1}\cos(\varphi_{F1}) - \sqrt{k^2_{F3} - k^2_{F1}[1 - \cos^2(\varphi_{F1})]}, \quad (5a)$$

$$\Delta k_{F3} = k_1 + k_3 - k_{F3}\cos(\varphi_{F3}) - \sqrt{k^2_{F1} - k^2_{F3}[1 - \cos^2(\varphi_{F3})]} \quad (5b)$$

for $\mathbf{k}_{F1}$ and $\mathbf{k}_{F3}$, respectively. Without taking the dark state into consideration, we can obtain the cone emissions of $\mathbf{k}_{F1}$ and $\mathbf{k}_{F3}$ based on Eqs. (3) and (4) as displayed in Fig. 2(b), in which the outer and inner cones represent $\mathbf{k}_{F1}$ and $\mathbf{k}_{F3}$, respectively. According to Eqs. (5a) and (5b), we display the phase mismatching $\Delta k_{F1,F3}(z = 10\ \mathrm{cm})$ versus transverse coordinates x and y in Fig. 2(c). As is well known, $\Delta k_{F1,F3} = 0$ (corresponding to the optimal phase-matching angle) means that the beams are completely phase matched, which leads to the largest efficiency to generate the SP-FWMs. According to Fig. 2(c), it is clear to see that $\Delta k_{F1,F3} = 0$ corresponds two rings (one for $\mathbf{k}_{F1}$ and the other for $\mathbf{k}_{F3}$), which can be called phase-matching rings. The generation coefficient will reduce greatly if $\Delta k_{F1,F3} \neq 0$, so the intensities of $\mathbf{k}_{F1}$ and $\mathbf{k}_{F3}$ are the largest on the phase-matching ring and

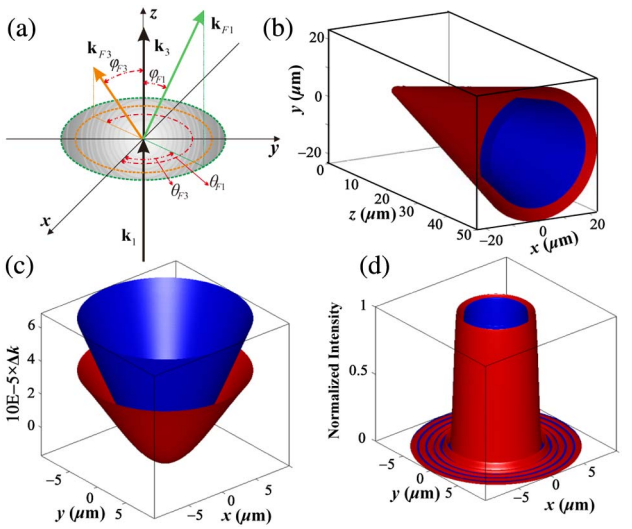

Fig. 2. (a) Geometric distribution of $\mathbf{k}_1$, $\mathbf{k}_3$, $\mathbf{k}_{F1}$, and $\mathbf{k}_{F3}$. (b) Cone emissions of $\mathbf{k}_{F1}$ (outer) and $\mathbf{k}_{F3}$ (inner). (c) Phase mismatching $\Delta k_{F1,F3}$ (x, y, $z = 10$ μm). (d) Normalized intensity corresponding to (c).

decrease sharply when deviating from this ring. To make this problem clear, we display the normalized intensities of $\mathbf{k}_{F1}$ and $\mathbf{k}_{F3}$ in Fig. 2(d). It can be seen that the peaks of the normalized gains are on the phase-matching rings that correspond to $\Delta k_{F1,F3} = 0$ in Fig. 2(c). With increasing propagation distance, the radii of the phase-matching rings also increase monotonically, so we can obtain the cone emissions shown in Fig. 2(b).

2. Phase-Conjugate FWM Cone Emission

In the ladder-type subsystem $|0\rangle - |1\rangle - |2\rangle$ (Fig. 1), two high intensity "pump" beams $\mathbf{k}_1$ and $\mathbf{k}_2$ drive two off-resonant transitions and induce two phase-conjugate FWMs $\mathbf{k}_{F1'}$ and $\mathbf{k}_{F2}$. The corresponding phase-matching configuration is shown in Fig. 3(a), according to which the phase mismatching conditions for $\mathbf{k}_{F1'}$ and $\mathbf{k}_{F2}$ can be obtained as

$$\Delta k_{F1'} = k_2 - k_1 - k_{F1'}\cos(\varphi_{F1'}) - \sqrt{k_{F2}^2 - k_{F1'}^2[1-\cos^2(\varphi_{F1'})]}, \tag{6a}$$

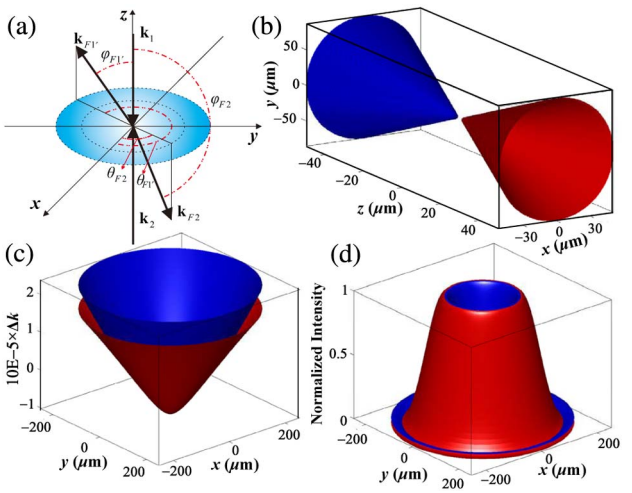

Fig. 3. Figure setup is as Fig. 2 but for phase-conjugate FWM processes. In (c), $z = 40$ μm.

$$\Delta k_{F2} = k_2 - k_1 - k_{F2}\cos(\varphi_{F2}) - \sqrt{k_{F1'}^2 - k_{F2}^2[1-\cos^2(\varphi_{F2})]}. \tag{6b}$$

Via the pathway $\rho_{00}^{(0)} \xrightarrow{\omega_1} \rho_{10}^{(1)} \xrightarrow{\omega_2} \rho_{20}^{(2)} \xrightarrow{-\omega_{F2}} \rho_{10F1}^{(3)}$ and considering the dressing effect of $\mathbf{k}_3$, the density matrix element for $\mathbf{k}_{F1'}$ can be written as

$$\rho_{F1'}^{(3)} = \frac{-iG_1G_2G_{F2}^*}{(d_{10} + |G_3|^2/d'_{30})d_{20}(d''_{10} + |G_3|^2/d''_{30})}, \tag{7}$$

where $d'_{30} = \Gamma_{30} + i(\Delta_1 - \Delta_3)$, $d''_{10} = \Gamma_{10} + i(\Delta_1 - \delta)$, and $d''_{30} = \Gamma_{30} + i(\Delta_1 - \Delta_3 - \delta)$. Similarly, the density matrix element for $\mathbf{k}_{F2}$ can be also obtained as

$$\rho_{F2}^{(3)} = \frac{-iG_1G_2G_{F4}^*}{(d_{10} + |G_3|^2/d_{30})d_{20}(d_{21} + |G_3|^2/d_{23})}, \tag{8}$$

where $d_{21} = \Gamma_{21} + i(\delta + \Delta_2)$ and $d_{23} = \Gamma_{23} + i(\Delta_2 \pm \Delta_3 + \delta)$.

Based on Eqs. (6)–(8), we display the cone emission of $\mathbf{k}_{F1'}$ and $\mathbf{k}_{F2}$ in Fig. 3(b), phase mismatching $\Delta k_{F1',F2}(z = 40$ μm) in Fig. 3(c), and the corresponding normalized intensities of $\mathbf{k}_{F1'}$ and $\mathbf{k}_{F2}$ in Fig. 3(d). Different from the self-diffraction FWM cone emission in Fig. 2(b), the phase-conjugate FWM cone emissions propagate along the opposite directions which are in accordance with the geometric distribution shown in Fig. 3(a). However, the phase mismatching and normalized intensities shown in Figs. 3(c) and 3(d) are similar to those of the self-diffraction case. The FWM generation efficiency will be the largest at the phase-matching rings $\Delta k_{F1',F2} = 0$, which can be also illustrated from Figs. 3(c) and 3(d). And the radii of the rings increase along the increment of the propagation distance, which make the $\mathbf{k}_{F1'}$ and $\mathbf{k}_{F2}$ cones form along the positive and negative propagation directions, respectively.

3. SINGLE-MODE SQUEEZING

In the above section, we have discussed the spatial properties of SP-FWM processes without injection. The conical emission disappears in a cavity, but if paired fields can be quantized, the squeezing between them still exists. So we can apply the basic theory about single-mode squeezing of twin beams in free space to intracavity theory. Furthermore, the parametric processes indicated in Section 2 will generate two spatial modes with certain directions (two signal channels), along which we launch the injections [15,22].

A. Amplitude and Phase

We study optical squeezing MWM in an atom–cavity coupling system consisting of atomic vapors confined in the four-mirror-formed mode volume with a length of $L_c = 17$ cm, as shown in Fig. 4. The mirrors M3 and M1 are input and output mirrors with a radius of 50 mm, the reflectance r_3 (r_1) and transmittance t_3 (t_1) of which fulfill the condition $r_i^2 + t_i^2 = 1$ ($i = 1, 3$), while M2 and M4 are high-reflection mirrors. Cavity frequency scanning and locking can be implemented by a piezoelectric transducer (PZT) behind M4. The length of the rubidium vapor cell including the Brewster windows is $L_a = 7$ cm. The cell is wrapped in μ-metal sheets to shield from external magnetic fields, and a heat tape is placed outside the sheets for controlling the temperature to influence

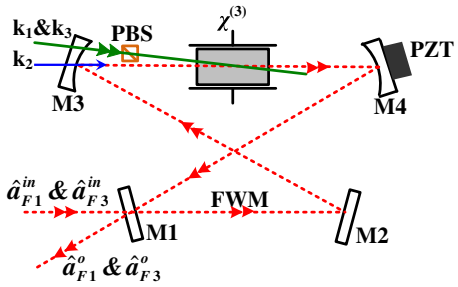

Fig. 4. Experimental scheme of single-mode squeezing. $\hat{a}^{o}_{F1}$ and $\hat{a}^{o}_{F3}$ are the amplified output FWM cavity modes; $\hat{a}^{\rm in}_{F1}$ and $\hat{a}^{\rm in}_{F3}$ are injected fields.

the atomic density. Since we do not consider Doppler effects in this paper, our analysis is also suitable for ring or standing-wave cavities [23].

In the cavity shown as Fig. 4, due to the assumption that the pump beams are undepleted, the intensities of the pump beams will be much larger than those of the SP-FWM signals. Thus, we can regard the pump beams as classical fields and quantize the two SP-FWM signals as $\hat{a}_{F1}$ and $\hat{a}_{F3}$. Owing to the same output direction and polarization, we regard $\hat{a}_{F1}$ and $\hat{a}_{F3}$ as one mode and use $\hat{a}_{F1}$ to represent both of them. Even though the self-diffraction FWM signals and their cavity modes are generated along the same direction, the polarizations of the two modes are perpendicular, so one can record them separately by putting a polarizer before the photodiode detectors.

Here, we introduce the nonlinear coefficient κ, which is proportional to the nonlinear optical susceptibility and amplitude of pump fields, to describe the nonlinear gain in the MWM process. We denote γ as the decay rate of the single-mode signal due to transmission of the input–output coupler mirror M1, γ_c due to all other intracavity losses, and $\hat{c}$ as the vacuum mode that is coupled into the single-mode signal through γ_c. So the motion equation can be obtained as [24]

$$\frac{d\hat{a}_{F1}}{dt} = -i\Delta\hat{a}_{F1} - (\gamma+\gamma_c)\hat{a}_{F1} + \kappa\hat{a}^{+}_{F1}\exp(i\theta_p) + \sqrt{2\gamma}\hat{a}^{\rm in}_{F1} + \sqrt{2\gamma_c}\hat{c}, \tag{9}$$

where θ_p is the relative phase between pump lights and the seeding lights, Δ is the cavity detuning, and $\hat{a}^{\rm in}_{F1}$ is the injected field. With the steady-state approximation and Fourier transformation (Ω is the analysis frequency), we can get $\hat{a}_{F1}$ with $\theta_p = 0$ as

$$\hat{a}_{F1} = \frac{(\gamma+\gamma_c - i\Omega - i\Delta)\left(\sqrt{2\gamma}\hat{a}^{\rm in}_{F1} + \sqrt{2\gamma_c}\hat{c}\right)}{(\gamma+\gamma_c)^2 + (\Delta+\Omega)^2 - \kappa^2} + \frac{\kappa\left(\sqrt{2\gamma}\hat{a}^{\rm in+}_{F1} + \sqrt{2\gamma_c}\hat{c}^{+}\right)}{(\gamma+\gamma_c)^2 + (\Delta+\Omega)^2 - \kappa^2}. \tag{10}$$

We can write the mean value of $\hat{a}_{F1}$ as $\langle\hat{a}_{F1}\rangle = a_1 + ia_2$, in which a_1 and a_2 are the real and imaginary parts, respectively. The amplitude and phase of the output field $\mathbf{k}_{F1}$ are

$$\alpha_{\rm in} = \sqrt{a_1^2 + a_2^2}, \qquad \varphi = \operatorname{atan}\left(\frac{a_2}{a_1}\right). \tag{11}$$

The mean values of $\hat{a}^{\rm in}_{F1}$ and coupling vacuum field $\hat{c}$ can be written as $\langle\hat{a}^{\rm in}_{F1}\rangle = \alpha_{\rm in}\exp(-i\phi^{\rm in}_{F1})$, $\langle\hat{c}^{+}\rangle = 1$ and $\langle\hat{c}\rangle = 0$, in which $\alpha_{\rm in}$ and $\phi^{\rm in}_{F1}$ are the amplitude and phase, respectively.

Now, we begin to investigate the intensity and phase of the output field, which can be well controlled by the frequency detunings of the dressing fields ($\mathbf{k}_2$ can be viewed as a dressing field if it is strong enough [12]) as well as the nonlinear coefficient κ. Here, we would like to emphasize that κ is proportional to the density matrix element. Therefore, the changing trend of κ reflects the changing trend of the density matrix element.

We study the dressing influences of $\mathbf{k}_2$ on the theoretical intensity and phase of the single-mode versus Δ at different Δ_1 when $\phi^{\rm in}_{F1} = 0$, which can be obtained based on Eqs. (9)–(11), and the results are illustrated by the solid curves in Fig. 5. The baseline of the intensities at $\Delta = 0$ is represented by the dashed curves in Figs. 5(a) and 5(b), which is the same with κ versus Δ_1.

When the power of $\mathbf{k}_2$ is strong enough, the baseline shows an AT splitting [Fig. 5(a)] due to its dressing effect. Based on the properties of κ, the output intensities (solid curves) show that the peak becomes higher and two dips shallower with κ increased. Each output spectrum has one peak and two dips, which is resulted from the constructive interference between the injected field and the pump fields [6]. One can control κ with AT splitting induced by the dressing effect of the $\mathbf{k}_2$, which results in the evolution of the output intensity at $\Delta = 0$ shown in Fig. 5(a). However, when the power of $\mathbf{k}_2$ is weak so that its dressing effect can be neglected, κ exhibits a single peak, and the evolution of the output at $\Delta = 0$ is shown in Fig. 5(b).

As for the phase of the single-mode, the distance of splitting share the same law with the intensity, which indicates a very steep variation of the anomalous dispersive profile and can result in fast light around $\Delta = 0$, which is opposite to the experimental results in Ref. [25] because of the different relative phase $\phi^{\rm in}_{F1}$. The phase of the output field shows that the gradient increases with a decrease in κ, as shown in Figs. 5(c) and 5(d). The variations in Fig. 5(c) are not very obvious because the influence of the dark state is relatively weak.

Then we study the influences of the dressing field $\mathbf{k}_2$ on the output intensity and phase of the single-mode at different Δ_2

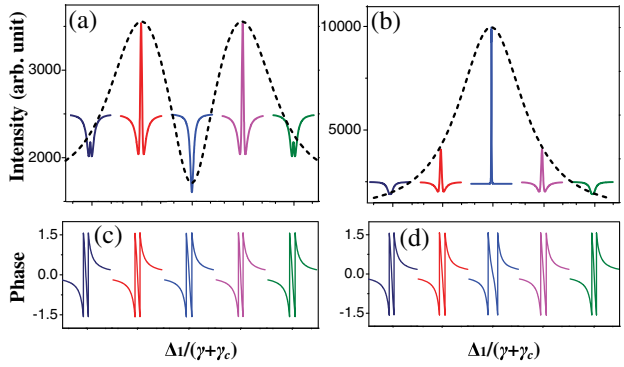

Fig. 5. Solid curves, (a) and (b) theoretical intensity and (c) and (d) phase of the single-mode versus $\Delta/(\gamma+\gamma_c) \in [-1010]$ at different Δ_1 (a) and (c) with and (b) and (d) without the dressing effect of $\mathbf{k}_2$. Parameters: $\phi^{\rm in}_{F1} = 0$, $\Delta_2 = 0$, and $\Delta_1/(\gamma+\gamma_c) = -40, -20, 0, 20, 40$, respectively, from left to right. Dashed curves, intensities at $\Delta = 0$ versus Δ_1.

with $\phi_{F1}^{\text{in}} = 0$ and $\Delta_1/(\gamma+\gamma_c) = -15$. The results are illustrated in Fig. 6. When $\Delta_1/(\gamma+\gamma_c) = -15$, the baselines of the intensities at $\Delta = 0$ are same with κ versus Δ_2, which are shown by the dashed curves in Fig. 6(a). The satisfied enhancement and suppression conditions in Fig. 6(a) are $\Delta_1 + \left(\Delta_2 + \sqrt{\Delta_2^2 + 4G_2^2}\right)/2 = 0$ and $\Delta_1 + \Delta_2 = 0$ [26,27], respectively, and the evolution of the output at $\Delta = 0$ is shown by the solid curves shown in Fig. 6(a). Without the dressing effect of $\mathbf{k}_2$, the intensities at $\Delta = 0$ do not change versus Δ_2, as shown in Fig. 6(b). For the phase shown in Figs. 6(c) and 6(d), we can obtain almost the same results as in Fig. 5.

B. Control Single-Mode Squeezing

Since the amplitude and phase of the SP-FWM can be adjusted by the dark state, we wonder whether the fluctuations of the SP-FWMs can be controlled or not. Therefore, we would like to discuss phase-sensitive squeezing, such that we define the amplitude quadrature $\hat{X}$ and phase quadrature $\hat{Y}$ as $\hat{X}_{F1}^{\theta_p} = \hat{a}_{F1}e^{-i\theta_p} + \hat{a}_{F1}^{+}e^{i\theta_p}$ and $\hat{Y}_{F1}^{\theta_p} = -i(\hat{a}_{F1}e^{-i\theta_p} - \hat{a}_{F1}^{+}e^{i\theta_p})$.

Considering the Fourier transform of the operators, the steady-state approximation $d\hat{X}_{F1}^{\theta_p}/dt = d\hat{Y}_{F1}^{\theta_p}/dt = 0$ and boundary condition $\hat{a}_{F1}^{o}(\Omega) = \sqrt{2\gamma}\hat{a}_{F1}(\Omega) - \hat{a}_{F1}^{\text{in}}(\Omega)$, we can obtain the amplitude and phase variances at $\theta_p = 0$ or $\theta_p = \pi$ as

$$\begin{aligned}\langle\delta^2\hat{X}_{F1}^{o}(\Omega)\rangle = (\{[(\gamma\pm\kappa)^2 - \gamma_c^2 + \Omega^2 - \Delta^2]^2 + 4\gamma_c^2\Omega^2\}\langle\delta^2\hat{X}_{F1}^{\text{in}}(\Omega)\rangle \\ + 4\gamma\gamma_c[(\gamma+\gamma_c\pm\kappa)^2 + \Omega^2]\langle\delta^2\hat{X}_c(\Omega)\rangle \\ + 4\gamma^2\Delta^2\langle\delta^2\hat{Y}_{F1}^{\text{in}}(\Omega)\rangle + 4\Delta^2\gamma\gamma_c\langle\delta^2\hat{Y}_c(\Omega)\rangle) \\ /\{[(\gamma+\gamma_c)^2 + \Delta^2 - \Omega^2 - \kappa^2]^2 + 4\Omega^2(\gamma+\gamma_c)^2\},\end{aligned} \tag{12a}$$

$$\begin{aligned}\langle\delta^2\hat{Y}_{F1}^{o}(\Omega)\rangle = (\{[(\gamma\mp\kappa)^2 - \gamma_c^2 + \Omega^2 - \Delta^2]^2 + 4\gamma_c^2\Omega^2\}\langle\delta^2\hat{Y}_{F1}^{\text{in}}(\Omega)\rangle \\ + 4\gamma\gamma_c[(\gamma+\gamma_c\mp\kappa)^2 + \Omega^2]\langle\delta^2\hat{Y}_c(\Omega)\rangle \\ + 4\gamma^2\Delta^2\langle\delta^2\hat{X}_{F1}^{\text{in}}(\Omega)\rangle + 4\Delta^2\gamma\gamma_c\langle\delta^2\hat{X}_c(\Omega)\rangle) \\ /\{[(\gamma+\gamma_c)^2 + \Delta^2 - \Omega^2 - \kappa^2]^2 + 4\Omega^2(\gamma+\gamma_c)^2\},\end{aligned} \tag{12b}$$

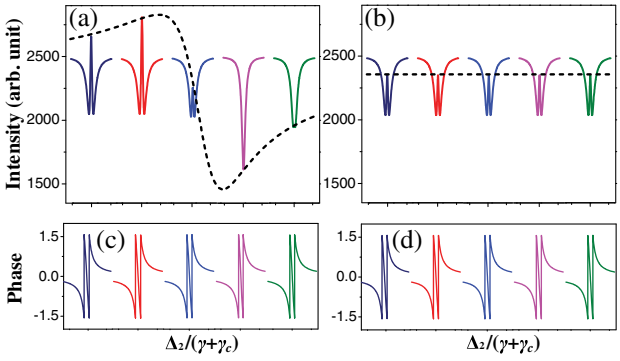

Fig. 6. Solid curves, (a) and (b) theoretical intensity and (c) and (d) phase of the single-mode versus $\Delta/(\gamma+\gamma_c) \in [-10\ 10]$ at different Δ_2 (a) and (c) with and (b) and (d) without the dressing effect from $\mathbf{k}_2$. Parameters: $\phi_{F1}^{\text{in}} = 0$, $\Delta_1/(\gamma+\gamma_c) = -15$, and $\Delta_2/(\gamma+\gamma_c) = -50, -15, 0, 15, 50$, respectively, from left to right. Dashed curves, intensities at $\Delta = 0$ versus Δ_2.

where the plus and minus symbols correspond to $\theta_p = 0$ and $\theta_p = \pi$, respectively.

We first investigate the quantum noise variances of the quadrature components of the output cavity mode by scanning $\Delta/(\gamma+\gamma_c)$ at different Δ_1 when the squeezed states are injected. Comparing the results with the shot-noise limit (SNL) [28,29] and the results obtained without pump lights, we can find the influence of κ with and without the dressing effect of $\mathbf{k}_2$ obviously. When one of the pump fields is blocked, the nonlinear process is not active. The quantum noise variances of the quadrature components are shown by the dotted-line in Fig. 7, and the injected squeezed vacuum states are shown by the first solid curve in each panel, which can be used as a reference to examine the nonlinear process inside the cavity of the input states.

Figures 7(a) and 7(b) illustrate the quantum noise variances of amplitudes and phases at $\theta_p = 0$ with the dressing effect of $\mathbf{k}_2$. While Figs. 7(c) and 7(d) correspond to the case without the dressing effect. We find that the quantum noise variance of phase quadrature is squeezed more at the resonance due to the nonlinear process, while the variance of amplitude quadrature becomes noisier than the input squeezed states. This phenomenon is in line with the Heisenberg uncertainty relationship [30,31]. It is clear that both the squeezing degree and the noise degree at $\Delta = 0$ can be modulated by Δ_1. Due to the dressing effect of $\mathbf{k}_2$, there are AT splittings for both the amplitude and phase quadrature noise variances, as shown in Figs. 7(a) and 7(b) rather than in Figs. 7(c) and 7(d).

When the nonlinear process is operated at $\theta_p = \pi$, the quantum noise variances of amplitudes and phases with (or without) the dressing effect of $\mathbf{k}_2$ are shown in Fig. 7(e) [or Fig. 7(g)] and Fig. 7(f) [or Fig. 7(h)]. The amplitude quadrature noise variances are changed from very noise to squeezed at resonance, as shown in Figs. 7(e) and 7(g). The squeezing degree of the corresponding phase quadrature noise variances at resonance decreases (even to noise), as shown in Figs. 7(f) and 7(h). Meanwhile, the profiles of the quadrature noise variance at resonance are opposite to those shown in Figs. 7(a)–7(d).

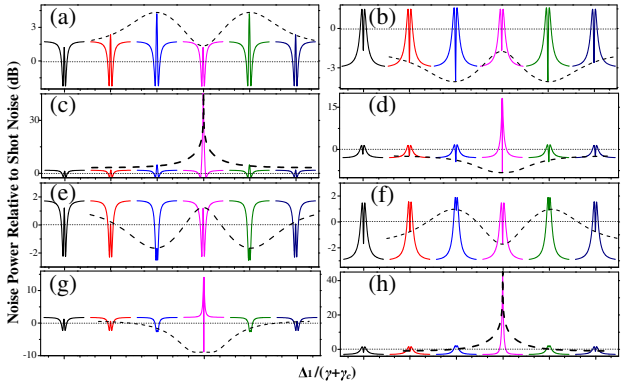

Fig. 7. Solid curves, theoretical single-mode squeezing versus $\Delta/(\gamma+\gamma_c) \in [-15\quad 15]$ at different Δ_1 when injecting squeezed states, $\theta_p = 0$ and $\Delta_2 = 0$, (a) and (b) with and (c) and (d) without the dressing effect of $\mathbf{k}_2$. The first curve is the noise power spectrum with one of the pump fields blocked and the following five curves, respectively, from left to right are noise power spectra with $\Delta_1/(\gamma+\gamma_c) = -40, -20, 0, 20, 40$. Dashed curves, noise variances at $\Delta = 0$. Dotted lines, SNL with vacuum states injected. (e)–(h) Same as (a)–(d) but with $\theta_p = \pi$.

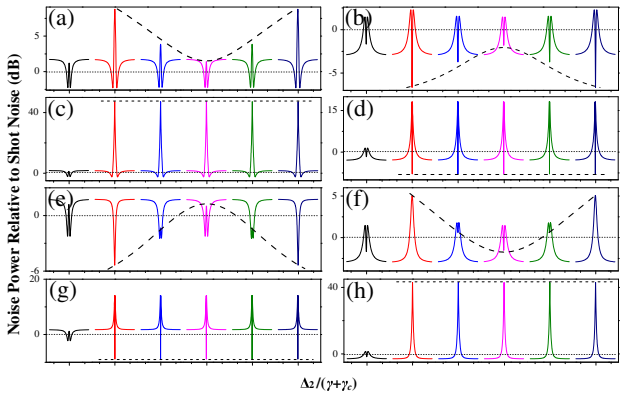

Fig. 8. (a)–(h) Figure setup is as Fig. 7 but with different Δ_2 and $\Delta_1 = 0$. The curves in (a)–(h) from left to right are the noise power spectrum with one of the pump fields blocked, $\Delta_2/(\gamma+\gamma_c) = -50, -15, 0, 15, 50$, respectively.

Now, we fix $\Delta_1 = 0$ and set different Δ_2 to investigate the quantum noise variances of the output quadrature components, as shown in Fig. 8. When $\theta_p = 0$, the increased noise degree of the amplitude quadrature variances at resonance shows a pure suppression with $\mathbf{k}_2$ dressed and a line without $\mathbf{k}_2$ dressed, which are the same with κ versus Δ_2, as displayed by the dashed curves in Figs. 8(a) and 8(c). The corresponding suppression condition satisfies $\Delta_1 + \Delta_2 = 0$. While the increased squeezing degree of the phase quadrature variances at resonance shows a pure enhancement and a line considering and not considering the dressing effect of $\mathbf{k}_2$, which are opposite to κ versus Δ_2, and shown in Figs. 8(b) and 8(d). When $\theta_p = \pi$, the phenomena shown in Figs. 8(e)–8(h) are totally opposite to those in Figs. 8(a)–8(d).

The results exhibited in Figs. 7 and 8 demonstrate that the squeezing degree can be adjusted by κ or the corresponding density matrix element. In other words, the squeezing degree can be controlled by the dark state. In addition, the squeezing can be converted via manipulating θ_p.

C. Intensity and Squeezing in Coupled Cavities

As coupled cavities would introduce more interesting squeezing processes and results [7], we study the reflection intensity and squeezing of the reflected field from the coupled cavities with the squeezed state injected.

The squeezed state generated by optical parametric oscillation (the configuration in Fig. 5 with the vacuum state injected, described as $\hat{a}_{F1}$) is injected into the coupled cavities shown in Fig. 9(a) through an optical isolator, which is used to separate the reflection field of the coupled cavities from the injected squeezed field. The coupled cavities are constructed by two directly coupled cavities C1 and C2. The complex reflectivity from the coupled cavities and the first cavity can be given as $R_1 = (r_1 - r_0 e^{i\phi_1})/(1 - r_0 r_1 e^{i\phi_1})$ and $R_2 = (r_2 - R_1 e^{i\varphi_2})/(1 - R_1 r_2 e^{i\phi_2})$, where φ_j are the round trip phase-shifts, r_j are the reflection indices of cavity mirrors, and $j = 1, 2$ specifies the first or second cavity. If we rewrite $R_2 = \rho(\varphi_1, \varphi_2) e^{i\theta(\varphi_1,\varphi_2)}$ with $\rho(\varphi_1, \varphi_2)$ and $\theta(\varphi_1, \varphi_2)$ being the amplitude and phase, respectively, the output field $\hat{a}_{\text{out}}(\Omega)$, which is reflected from the coupled cavities, can be expressed as

$$\hat{a}_{\text{out}}(\Omega) = \rho(\varpi_{F1} + \Omega) e^{i\theta(\varpi_{F1}+\Omega)} \hat{a}_{F1}(\Omega) + \sqrt{1 - \rho^2(\varpi_{F1} + \Omega)}\,\hat{c}(\Omega), \tag{13}$$

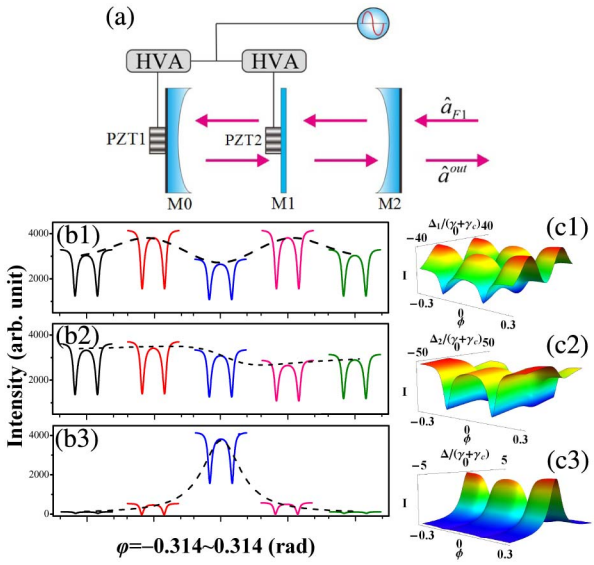

Fig. 9. (a) Coupled cavities constructed by mirrors M0, M1, and M2, which form two standing wave cavities C1 and C2. The cavity length of C1 and C2 can be controlled by PZT 1 and 2, respectively. (b) Solid curves, theoretical reflection intensity of the coupled cavities with the squeezed signal beam injected, versus the round trip phase-shift $\varphi = \varphi_1 = \varphi_2$ with $\Omega = 0$, $r_0 > 99\%$, $r_1 = 99.8\%$, and $r_2 = 96.8\%$. (b1) With $\Delta_1/(\gamma+\gamma_c) = -40, -20, 0, 20, 40$, respectively, from left to right, $\Delta_2 = \Delta = 0$ under the dressing effect of $\mathbf{k}_2$. (b2) with $\Delta_2/(\gamma+\gamma_c) = -50, -25, 0, 25, 50$, respectively, from left to right, $\Delta_1/(\gamma+\gamma_c) = -15$ and $\Delta = 0$. (b3) With $\Delta/(\gamma+\gamma_c) = -5, -2.5, 0, 2.5, 5$, respectively, from left to right, $\Delta_1/(\gamma+\gamma_c) = -20$ and $\Delta_2 = 0$. Dashed curves, baselines. (c1)–(c3) 3D simulations corresponding to (b1)–(b3).

where $\hat{c}$ is the coupled vacuum field due to cavity loss. So, the photon number of the reflected field in the frequency domain can be obtained by

$$\langle \hat{a}^+_{\text{out}}(-\Omega)\hat{a}_{\text{out}}(\Omega)\rangle = \rho(\varpi_{F1} - \Omega)\rho(\varpi_{F1} + \Omega) e^{-i[\theta(\varpi_{F1}-\Omega) - \theta(\varpi_{F1}+\Omega)]} \times \langle \hat{a}^+_{F1}(-\Omega)\hat{a}_{F1}(\Omega)\rangle. \tag{14}$$

The intensity of the reflected field is proportional to the photon number, so we study the photon number instead of intensity.

Similar to the method used above for single-mode squeezing, the variances of the amplitude and phase quadratures for the coupled cavities can be obtained as

$$\begin{aligned}
&\langle \delta^2 \hat{X}_{\text{out}}(\Omega)\rangle \\
&= \frac{1}{4}\big|\rho(\varpi_{F1} + \Omega)\exp[i\theta(\varpi_{F1} + \Omega)] \\
&\quad + \rho(\varpi_{F1} - \Omega)\exp[-i\theta(\varpi_{F1} - \Omega)]\big|^2 \langle \delta^2 \hat{X}_{F1}(\Omega)\rangle \\
&\quad + \frac{1}{4}\big|\rho(\varpi_{F1} + \Omega)\exp[i\theta(\varpi_{F1} + \Omega)] \\
&\quad - \rho(\varpi_{F1} - \Omega)\exp[-i\theta(\varpi_{F1} - \Omega)]\big|^2 \langle \delta^2 \hat{Y}_{F1}(\Omega)\rangle \\
&\quad + \frac{1}{4}\left|\sqrt{1 - \rho^2(\varpi_{F1} + \Omega)} + \sqrt{1 - \rho^2(\varpi_{F1} - \Omega)}\right|^2 \langle \delta^2 \hat{X}_c(\Omega)\rangle \\
&\quad + \frac{1}{4}\left|\sqrt{1 - \rho^2(\varpi_{F1} + \Omega)} - \sqrt{1 - \rho^2(\varpi_{F1} - \Omega)}\right|^2 \langle \delta^2 \hat{Y}_c(\Omega)\rangle,
\end{aligned} \tag{15a}$$

$$\langle \delta^2 \hat{Y}_{\text{out}}(\Omega)\rangle$$
$$= \frac{1}{4}|-\rho(\varpi_{F1}+\Omega)\exp[i\theta(\varpi_{F1}+\Omega)]$$
$$+\rho(\varpi_{F1}-\Omega)\exp[-i\theta(\varpi_{F1}-\Omega)]|^2\langle\delta^2\hat{X}_{F1}(\Omega)\rangle$$
$$+\frac{1}{4}|\rho(\varpi_{F1}+\Omega)\exp[i\theta(\varpi_{F1}+\Omega)]$$
$$+\rho(\varpi_{F1}-\Omega)\exp[-i\theta(\varpi_{F1}-\Omega)]|^2\langle\delta^2\hat{Y}_{F1}(\Omega)\rangle$$
$$+\frac{1}{4}\left|-\sqrt{1-\rho^2(\varpi_{F1}+\Omega)}+\sqrt{1-\rho^2(\varpi_{F1}-\Omega)}\right|^2\langle\delta^2\hat{X}_c(\Omega)\rangle$$
$$+\frac{1}{4}\left|\sqrt{1-\rho^2(\varpi_{F1}+\Omega)}+\sqrt{1-\rho^2(\varpi_{F1}-\Omega)}\right|^2\langle\delta^2\hat{Y}_c(\Omega)\rangle. \quad (15b)$$

We first show the dressing influences of $\mathbf{k}_2$ on the reflection intensity of the coupled cavities versus the round trip phase-shift φ based on Eq. (14). The term $\langle\hat{a}^+_{F1}(-\Omega)\hat{a}_{F1}(\Omega)\rangle$ in Eq. (14) expresses the output intensity with the vacuum state injected from the cavity configuration in Fig. 4, which is same as the results displayed in Figs. 5 and 6. The baselines of the intensity, as the dashed curves illustrated in Figs. 9(b1) and 9(b2), show AT splitting versus $\Delta_1/(\gamma+\gamma_c)$ and left-enhancement-right-suppression versus $\Delta_2/(\gamma+\gamma_c)$, respectively, because of the dressing effect of $\mathbf{k}_2$. However, the baseline, as the dashed curve shown in Fig. 9(b3), displays a single peak versus $\Delta/(\gamma+\gamma_c)$, which can be obtained obviously by the curve at $\Delta_1/(\gamma+\gamma_c)=-20$ in Fig. 5(a). The function of the coupled cavities split the original one mode into two modes [7], as shown by the solid curves in Figs. 9(b1)–9(b3). The corresponding three-dimensional simulations are shown in Figs. 9(c1)–9(c3).

Then we illustrate the quantum noise variances of the amplitude quadrature Eq. (15a) for the reflection signal of the coupled cavities with the squeezed state injected, as shown in Fig. 10. We can obtain the splitting of the original squeezed signal (see Fig. 5), which is induced by the coupled cavities and similar to the reflection intensity. The profile of the baselines of each variance at different Δ_1, shown as the dashed curve in Fig. 10, is an AT splitting versus Δ_1, because the noise degree of the amplitude quadrature of the squeezed state generated from the cavity (Fig. 4) at $\Delta=0$ is proportional to κ, which is induced by the dressing effect of $\mathbf{k}_2$. Therefore, the squeezing degree for the reflection signal of the coupled cavities can be controlled by the dark state.

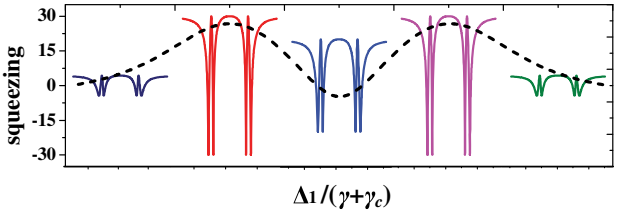

Fig. 10. Solid curves, theoretical squeezing of the amplitude quadrature for the reflection signal of the coupled cavities with an injected squeezed beam versus the round trip phase-shift $\varphi=\varphi_1=\varphi_2\in[-0.2\quad 0.2]$ with $\Omega=0$, $\Delta_1/(\gamma+\gamma_c)=-40,-20,0,20,40$, respectively, from left to right, $\Delta_2=\Delta=0$ under the dressing effect of $\mathbf{k}_2$. Dashed curve, the roughly changing trend of the baseline/squeezing versus Δ_1.

4. TWO-MODE SQUEEZING

In the phase-conjugate SP-FWM process, the generated SP-FWM fields ($\mathbf{k}_{F1'}$ and $\mathbf{k}_{F2}$) are treated as two quantum fields (described as $\hat{a}_{F1'}$ and $\hat{a}_{F2}$). As depicted in Fig. 11(a), $\mathbf{k}_1$ and $\mathbf{k}_2$ are generated along different directions, so we can treat the two SP-FWMs as two modes ($\hat{a}^o_{F1'}$ and $\hat{a}^o_{F2}$), which can be detected by two photodiode detectors. To measure the quadrature components, one needs to use the balanced homodyne detectors. Here, it is worth mentioning that there also can exist another kind of two FWM cavity modes that are along the same direction but with different polarizations. The corresponding diagram is similar to that shown in Fig. 4, in which the two fields ($\mathbf{k}_1$ and $\mathbf{k}_3$) with different polarizations are along the same direction.

The two SP-FWMs can be both amplified by injecting pump fields in the same intracavity FWM channel, which is described by the nonlinear coefficient κ. So the motion equations for $\mathbf{k}_{F1'}$ and $\mathbf{k}_{F2}$ can be written as [24]

$$\frac{d\hat{a}_{F1'}}{dt}=-i\Delta\hat{a}_{F1'}-(\gamma+\gamma_c)\hat{a}_{F1'}+\kappa\hat{a}^+_{F2}\exp(i\theta_p)$$
$$+\sqrt{2\gamma}\hat{a}^{\text{in}}_{F1'}+\sqrt{2\gamma_c}\hat{c}_1, \quad (16a)$$

$$\frac{d\hat{a}_{F2}}{dt}=-i\Delta\hat{a}_{F2}-(\gamma+\gamma_c)\hat{a}_{F2}+\kappa\hat{a}^+_{F1'}\exp(i\theta_p)$$
$$+\sqrt{2\gamma}\hat{a}^{\text{in}}_{F2}+\sqrt{2\gamma_c}\hat{c}_2, \quad (16b)$$

where $\hat{c}_1$ and $\hat{c}_2$ are the vacuum modes.

As shown by the energy level system in Fig. 11(b), if all the coupling beams are open, we can get two FWM signals ($\mathbf{k}'_{F2}$ and $\mathbf{k}'_{F3}$) and two SWM signals ($\mathbf{k}'_{S2}$ and $\mathbf{k}'_{S3}$), which satisfy $\mathbf{k}'_{F2}=\mathbf{k}_1+\mathbf{k}_2-\mathbf{k}'_2$, $\mathbf{k}'_{F3}=\mathbf{k}_1+\mathbf{k}_3-\mathbf{k}'_3$, $\mathbf{k}'_{S2}=\mathbf{k}_1+\mathbf{k}_2-\mathbf{k}'_2-\mathbf{k}_3+\mathbf{k}_3$, and $\mathbf{k}'_{S3}=\mathbf{k}_1+\mathbf{k}_3-\mathbf{k}'_3-\mathbf{k}_2+\mathbf{k}_2$, respectively. If we use the generated MWM signals as the injected fields which are injected into the FWM cavity mode channels shown in Fig. 11(a), we can get the $\chi^{(3)}$-$\chi^{(3)}$ cascade nonlinear process (inject $\mathbf{k}'_{F2}$ and $\mathbf{k}'_{F3}$) or the $\chi^{(5)}$-$\chi^{(3)}$ cascade nonlinear process (inject $\mathbf{k}'_{S2}$ and $\mathbf{k}'_{S3}$) to make the conjugate FWM cavity modes obtain optical parametric amplification [15]. Considering that we just use SWM signals as the injected fields to get the $\chi^{(5)}$-$\chi^{(3)}$ cascade nonlinear process, we only show the density matrix elements for SWM signals as

$$\rho^{(5)\text{in}}_{S2}=\frac{-iG_1G_2G'^*_2G_3G^*_3}{d^3_{10}d_{20}d_{30}},\qquad \rho^{(5)\text{in}}_{S3}=\frac{-iG_1G_3G'^*_3G_2G^*_2}{d^3_{10}d_{30}d_{20}}, \quad (17)$$

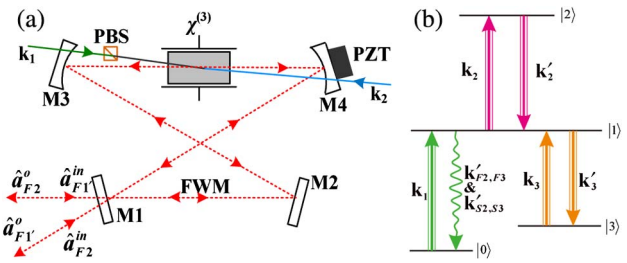

Fig. 11. (a) Schematics of two-mode squeezing with fields $\mathbf{k}_1$ and $\mathbf{k}_2$ passing through the atomic vapor along opposite directions. $\hat{a}^o_{F1'}$ and $\hat{a}^o_{F2}$ are the amplified output FWM cavity modes; $\hat{a}^{\text{in}}_{F1'}$ and $\hat{a}^{\text{in}}_{F2}$ correspond to the injected $\mathbf{k}'_{S3}$ and $\mathbf{k}'_{S2}$, respectively. (b) Inverted-Y-type energy level to produce MWM signals.

from the pathways

$$\rho_{00}^{(0)} \xrightarrow{\omega_1} \rho_{10}^{(1)} \xrightarrow{\omega_2} \rho_{20}^{(2)} \xrightarrow{-\omega_2} \rho_{10}^{(3)} \xrightarrow{-\omega_3} \rho_{30}^{(4)} \xrightarrow{\omega_3} \rho_{10S2}^{(5)\text{in}},$$
$$\rho_{00}^{(0)} \xrightarrow{\omega_1} \rho_{10}^{(1)} \xrightarrow{-\omega_3} \rho_{30}^{(2)} \xrightarrow{\omega_3} \rho_{10}^{(3)} \xrightarrow{\omega_2} \rho_{20}^{(4)} \xrightarrow{-\omega_2} \rho_{10S3}^{(5)\text{in}}.$$

As for the quantum noise variance of the amplitude quadrature summation, phase quadrature summation, amplitude quadrature difference, and phase quadrature difference of the two SP-FWM beams can be deduced as following:

$$\begin{aligned}\langle \delta^2 \hat{X}^o_{F1'+F2}(\Omega)\rangle = &(\{[(\gamma \pm \kappa)^2 - \gamma_c^2 + \Omega^2 - \Delta^2]^2 \\ &+ 4\gamma_c^2\Omega^2\}\langle \delta^2 \hat{X}^{\text{in}}_{F1'+F2}(\Omega)\rangle + 4\gamma^2\Delta^2\langle \delta^2 \hat{Y}^{\text{in}}_{F1'+F2}(\Omega)\rangle \\ &+ 4\gamma\gamma_c[(\gamma+\gamma_c \pm \kappa)^2 + \Omega^2]\langle \delta^2 \hat{X}^{\text{in}}_{c1+c2}(\Omega)\rangle \\ &+ 4\Delta^2\gamma\gamma_c\langle \delta^2 \hat{Y}^{\text{in}}_{c1+c2}(\Omega)\rangle) \\ &/\{[(\gamma+\gamma_c)^2 + \Delta^2 - \Omega^2 - \kappa^2]^2 + 4\Omega^2(\gamma+\gamma_c)^2\},\end{aligned} \tag{18a}$$

$$\begin{aligned}\langle \delta^2 \hat{Y}^o_{F1'+F2}(\Omega)\rangle = &(\{[(\gamma \mp \kappa)^2 - \gamma_c^2 + \Omega^2 - \Delta^2]^2 \\ &+ 4\gamma_c^2\Omega^2\}\langle \delta^2 \hat{Y}^{\text{in}}_{F1'+F2}(\Omega)\rangle + 4\gamma^2\Delta^2\langle \delta^2 \hat{X}^{\text{in}}_{F1'+F2}(\Omega)\rangle \\ &+ 4\gamma\gamma_c[(\gamma+\gamma_c \mp \kappa)^2 + \Omega^2]\langle \delta^2 \hat{Y}^{\text{in}}_{c1+c2}(\Omega)\rangle \\ &+ 4\Delta^2\gamma\gamma_c\langle \delta^2 \hat{X}^{\text{in}}_{c1+c2}(\Omega)\rangle) \\ &/\{[(\gamma+\gamma_c)^2 + \Delta^2 - \Omega^2 - \kappa^2]^2 + 4\Omega^2(\gamma+\gamma_c)^2\},\end{aligned} \tag{18b}$$

$$\begin{aligned}\langle \delta^2 \hat{X}^o_{F1'-F2}(\Omega)\rangle = &(\{[(\gamma \mp \kappa)^2 - \gamma_c^2 + \Omega^2 - \Delta^2]^2 \\ &+ 4\gamma_c^2\Omega^2\}\langle \delta^2 \hat{X}^{\text{in}}_{F1'-F2}(\Omega)\rangle + 4\gamma^2\Delta^2\langle \delta^2 \hat{Y}^{\text{in}}_{F1'-F2}(\Omega)\rangle \\ &+ 4\gamma\gamma_c[(\gamma+\gamma_c \mp \kappa)^2 + \Omega^2]\langle \delta^2 \hat{X}^{\text{in}}_{c1-c2}(\Omega)\rangle \\ &+ 4\Delta^2\gamma\gamma_c\langle \delta^2 \hat{Y}^{\text{in}}_{c1-c2}(\Omega)\rangle) \\ &/\{[(\gamma+\gamma_c)^2 + \Delta^2 - \Omega^2 - \kappa^2]^2 + 4\Omega^2(\gamma+\gamma_c)^2\},\end{aligned} \tag{18c}$$

$$\begin{aligned}\langle \delta^2 \hat{Y}^o_{F1'-F2}(\Omega)\rangle = &(\{[(\gamma \pm \kappa)^2 - \gamma_c^2 + \Omega^2 - \Delta^2]^2 \\ &+ 4\gamma_c^2\Omega^2\}\langle \delta^2 \hat{Y}^{\text{in}}_{F1'-F2}(\Omega)\rangle + 4\gamma^2\Delta^2\langle \delta^2 \hat{X}^{\text{in}}_{F1'-F2}(\Omega)\rangle \\ &+ 4\gamma\gamma_c[(\gamma+\gamma_c \pm \kappa)^2 + \Omega^2]\langle \delta^2 \hat{Y}^{\text{in}}_{c1-c2}(\Omega)\rangle \\ &+ 4\Delta^2\gamma\gamma_c\langle \delta^2 \hat{X}^{\text{in}}_{c1-c2}(\Omega)\rangle) \\ &/\{[(\gamma+\gamma_c)^2 + \Delta^2 - \Omega^2 - \kappa^2]^2 + 4\Omega^2(\gamma+\gamma_c)^2\}.\end{aligned} \tag{18d}$$

The amplitude quadrature summation is same as the phase quadrature difference, and the amplitude quadrature difference is same as the phase quadrature summation [24], so only two parts of Eq. (18) are independent. Therefore, we can just use Eqs. (18a) and (18b) to exhibit the amplification or squeezing of the summation and difference of the quadratures. For the injected fields, we adopt coherent fields and Einstein–Podolsky–Rosen (EPR) fields, respectively.

The curves in Figs. 12(a)–12(d) illustrate the quantum noise variances of the amplitude and phase quadrature summation of two SP-FWM modes versus Δ with $\Delta_1/(\gamma+\gamma_c) = -40, -20, 0, 20,$ and 40, respectively, from left to right. The dashed curves show the corresponding quantum noise variances versus Δ_1 with $\Delta = 0$. Comparing the squeezing results with SNL, which is shown by the first curve in each panel, the influence of the coupling coefficient on the squeezing is obvious. According to the Heisenberg uncertainty relationship, when the quantum noise variance of the amplitude quadrature [Fig. 12(a)] becomes noisier and shows an AT splitting profile, the variance of the phase quadrature [Fig. 12(b)] will be squeezed and exhibits a reverse AT splitting shape. The results in Figs. 12(c) and 12(d) are under the same conditions as those in Figs. 12(a) and 12(b), except without the dressing effect from $\mathbf{k}_3$. Clearly, the AT splitting in amplitude quadrature as well as the reverse AT splitting in phase quadrature disappears, however, the quantum noise variances of the amplitude and phase quadratures still will become noisier and be squeezed, respectively. In comparison with the cases with and without the dressing effect, we can see that the dark state can effectively control the squeezing process.

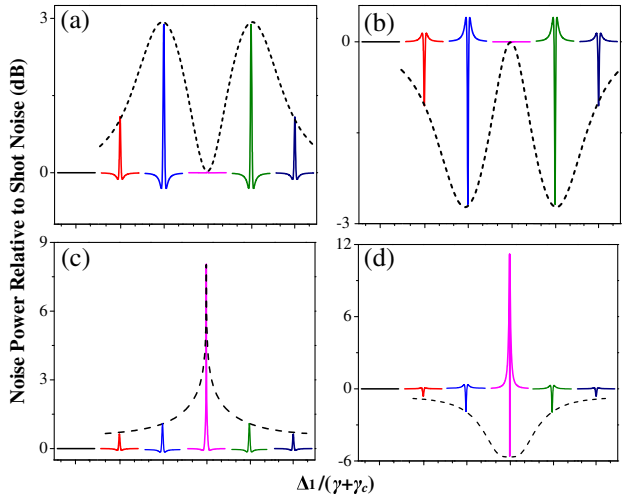

Fig. 12. Solid curves, theoretically calculated two-mode squeezing based on Eqs. (18a) and (18b) versus $\Delta/(\gamma+\gamma_c) \in [-15 \quad 15]$ at different Δ_1 when injecting coherent fields $\mathbf{k}'_{S3}$ and $\mathbf{k}'_{S2}$, (a) and (b) with and (c) and (d) without the dressing effect of $\mathbf{k}_3$. The first curve is the noise power spectrum with one of the pump fields blocked and the following five curves from left to right are the noise power spectra with $\Delta_3 = 0$ and $\Delta_1/(\gamma+\gamma_c) = -40, -20, 0, 20, 40,$ respectively. Dashed curves, noise variances versus Δ_1.

Then we study the influence of the dark state induced by the dressing effect of $\mathbf{k}_3$ on the squeezing degree with $\Delta_1/(\gamma+\gamma_c) = 15$ and $\Delta_1 = 0$, as shown in Figs. 13(a)–13(d) and Figs. 13(e)–13(h), respectively. The first curve in each panel displays the result of blocking one pump field, while the following five curves correspond to the results obtained at $\Delta_3/(\gamma+\gamma_c) = -50, -15, 0, 15,$ and 50 by injecting coherent fields. The profiles of quantum noise variances of the amplitude quadrature summation and phase quadrature summation at $\Delta = 0$ are depicted by the dashed curves, which are the corresponding variances versus $\Delta_3/(\gamma+\gamma_c)$, are the same as κ, and can be controlled by the dark state.

When $\Delta_1/(\gamma+\gamma_c) = 15$ [Fig. 13(a)], the quantum noise variance of the amplitude quadrature becomes noisier and shows enhancement in the region $\Delta_3 < 0$ and suppression in $\Delta_3 > 0$. The corresponding enhancement and suppression conditions are $\Delta_1 - \left(\Delta_3 + \sqrt{\Delta_3^2 + 4G_3^2}\right)/2 = 0$ and $\Delta_1 = \Delta_3$, respectively. As mentioned above, the quantum noise variance of

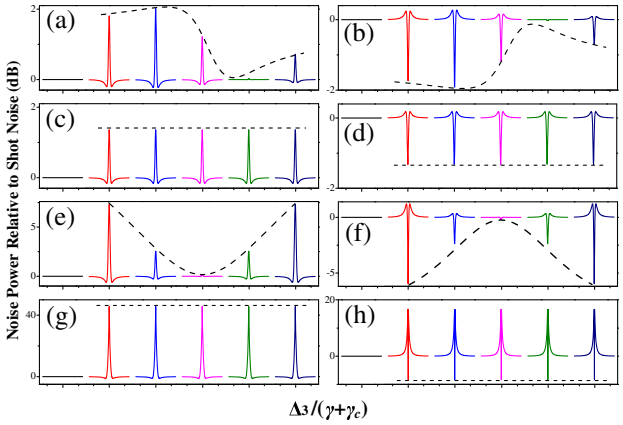

Fig. 13. Figure setup is as Fig. 12 but with different Δ_3 and $\Delta_1/(\gamma+\gamma_c)=15$ in (a)–(d) [$\Delta_1=0$ in (e)–(h)]. The right five solid curves correspond to $\Delta_3/(\gamma+\gamma_c)=-50,-15,0,15,50$, respectively.

the phase quadrature shown in Fig. 13(b) is squeezed and shows suppression in $\Delta_3<0$ and enhancement in $\Delta_3>0$, which is opposite to that shown in Fig. 13(a). The results indicate that the squeezing degree is proportional to κ. When the power of $\mathbf{k}_3$ is relatively weak, the dressing effect can be neglected, so it does not change the quantum noise variances of the amplitude and phase quadratures [Figs. 13(c) and 13(d)].

For the case $\Delta_1=0$, we take the same method to study the influence of the dark state on the intensity of the two-mode. As shown in Figs. 13(e) and 13(f), the quantum noise variances of the amplitude and phase quadratures exhibit a pure suppression and a pure enhancement, respectively. It is worth mentioning that the suppression condition is also $\Delta_1=\Delta_3$. If the dressing effect of $\mathbf{k}_3$ can be neglected, the quantum noise variances are also not affected, as shown in Figs. 13(g) and 13(h). Comparing the results shown in Figs. 13(a)–13(h), it is clear to see that the squeezing can be controlled by the dark state.

If an EPR fields is injected, the results are shown in Fig. 14, from which we find that the squeezing can be also controlled by the dressing effect of $\mathbf{k}_3$; by adjusting θ_p from 0 to π, the quantum noise variances of amplitude (phase) quadrature summation can be also converted from noise (squeezing) to squeezing (noise).

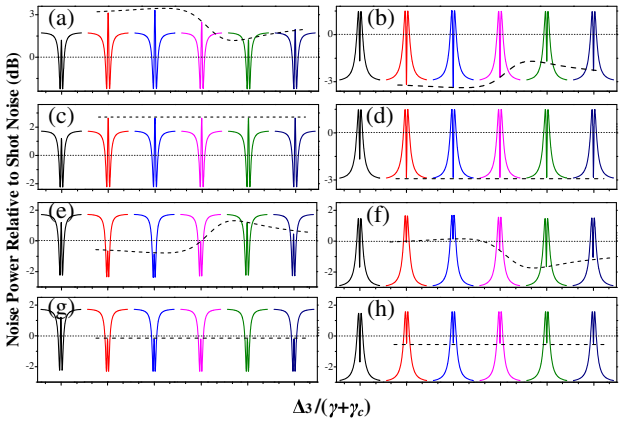

Fig. 14. Figure setup is as Fig. 13 but with EPR fields injected and $\Delta_1/(\gamma+\gamma_c)=15$ for all the cases. $\theta_p=0$ in (a)–(d) and $\theta_p=\pi$ in (e)–(h).

5. CONCLUSION

In summary, we have theoretically investigated the single-mode and two-mode quantum noise squeezing of MWM signals in a cavity filled with rubidium vapors. The cone emissions of the self-diffraction and phase-conjugate SP-FWM signals are studied without injected fields. When a coherent field and an EPR field are injected into the SP-MWM channels, they will undergo the $\chi^{(5)}$-$\chi^{(3)}$ cascade optical parametric amplification process and form cavity modes if the amplified MWM signals can be resonant with the cavity. It is found that the quantum noise of the cavity MWM modes may not only be squeezed but also amplified, and this kind of quantum process can be manipulated (enhanced or suppressed) by the dark state through the introduction of dressing effects. It is also demonstrated that if the quantum noise variance of the amplitude quadrature is squeezed, that of the phase quadrature will be amplified, and vice versa. The investigations have potential applications in quantum communications and signal processing.

ACKNOWLEDGMENTS

This work was supported by the 973 Program (2012CB921804), CPSF (2014T70923, 2012M521773), NSFC (11474228, 61308015, 11104214, 61108017, 11104216, 61205112), NSFCSP (2014JQ8341), XJTUIT (cxtd2014003), and KSTITSP (2014KCT-10).

REFERENCES

1. R. E. Slusher, L. W. Hollberg, B. Yurke, J. C. Mertz, and J. F. Valley, "Observation of squeezed states generated by four-wave mixing in an optical cavity," Phys. Rev. Lett. **55**, 2409–2412 (1985).
2. R. E. Slusher, P. Grangier, A. LaPorta, B. Yurke, and M. J. Potasek, "Pulsed squeezed light," Phys. Rev. Lett. **59**, 2566–2569 (1987).
3. V. Boyer, A. M. Marino, R. C. Pooser, and P. D. Lett, "Entangled images from four-wave mixing," Science **321**, 544–547 (2008).
4. A. M. Marino, R. C. Pooser, V. Boyer, and P. D. Lett, "Tunable delay of Einstein–Podolsky–Rosen entanglement," Nature **457**, 859–862 (2009).
5. Y. Shang, X. Jia, Y. Shen, C. Xie, and K. Peng, "Continuous variable entanglement enhancement and manipulation by a sub-threshold type ii optical parametric amplifier," Opt. Lett. **35**, 853–855 (2010).
6. H. Ma, C. Ye, D. Wei, and J. Zhang, "Coherence phenomena in the phase-sensitive optical parametric amplification inside a cavity," Phys. Rev. Lett. **95**, 233601 (2005).
7. K. Di, C. Xie, and J. Zhang, "Coupled-resonator-induced transparency with a squeezed vacuum," Phys. Rev. Lett. **106**, 153602 (2011).
8. S. E. Harris, "Electromagnetically induced transparency," Phys. Today **50**(7), 36–42 (1997).
9. M. Fleischhauer, A. Imamoglu, and J. P. Marangos, "Electromagnetically induced transparency: optics in coherent media," Rev. Mod. Phys. **77**, 633–673 (2005).
10. Y. Zhang, A. W. Brown, and M. Xiao, "Opening four-wave mixing and six-wave mixing channels via dual electromagnetically induced transparency windows," Phys. Rev. Lett. **99**, 123603 (2007).
11. Y. Zhang, U. Khadka, B. Anderson, and M. Xiao, "Temporal and spatial interference between four-wave mixing and six-wave mixing channels," Phys. Rev. Lett. **102**, 013601 (2009).
12. C. Li, H. Zheng, Y. Zhang, Z. Nie, J. Song, and M. Xiao, "Observation of enhancement and suppression in four-wave mixing processes," Appl. Phys. Lett. **95**, 041103 (2009).
13. Y. Zhang, Z. Nie, Z. Wang, C. Li, F. Wen, and M. Xiao, "Evidence of Autler–Townes splitting in high-order nonlinear processes," Opt. Lett. **35**, 3420–3422 (2010).

14. Y. Zhang, Z. Nie, Y. Zhao, C. Li, R. Wang, J. Si, and M. Xiao, "Modulated vortex solitons of four-wave mixing," Opt. Express **18**, 10963–10972 (2010).
15. H. Zheng, X. Zhang, Z. Zhang, Y. Tian, H. Chen, C. Li, and Y. Zhang, "Parametric amplification and cascaded-nonlinearity processes in common atomic system," Sci. Rep. **3**, 1885 (2013).
16. K. Bencheikh, E. Huntziger, and J. A. Levenson, "Quantum noise reduction in quasi-phase-matched optical parametric amplification," J. Opt. Soc. Am. B **12**, 847–852 (1995).
17. J. Wen, S. Du, Y. Zhang, M. Xiao, and M. H. Rubin, "Nonclassical light generation via a four-level inverted-Y system," Phys. Rev. A **77**, 033816 (2008).
18. T. Gantsog and R. Tanaś, "Phase properties of the two-mode squeezed vacuum states," Phys. Lett. A **152**, 251–256 (1991).
19. G. J. Milburn and S. L. Braunstein, "Quantum teleportation with squeezed vacuum states," Phys. Rev. A **60**, 937–942 (1999).
20. T. Hiroshima, "Decoherence and entanglement in two-mode squeezed vacuum states," Phys. Rev. A **63**, 022305 (2001).
21. P. M. Anisimov, G. M. Raterman, A. Chiruvelli, W. N. Plick, S. D. Huver, H. Lee, and J. P. Dowling, "Quantum metrology with two-mode squeezed vacuum: parity detection beats the Heisenberg limit," Phys. Rev. Lett. **104**, 103602 (2010).
22. H. Chen, Y. Zhang, X. Yao, Z. Wu, X. Zhang, Y. Zhang, and M. Xiao, "Parametrically amplified bright-state polariton of four- and six-wave mixing in an optical ring cavity," Sci. Rep. **4**, 3619 (2014).
23. J. Yuan, W. Feng, P. Li, X. Zhang, Y. Zhang, H. Zheng, and Y. Zhang, "Controllable vacuum Rabi splitting and optical bistability of multi-wave-mixing signal inside a ring cavity," Phys. Rev. A **86**, 063820 (2012).
24. H. Chen and J. Zhang, "Phase-sensitive manipulations of the two-mode entangled state by a type-ii nondegenerate optical parametric amplifier inside an optical cavity," Phys. Rev. A **79**, 063826 (2009).
25. C. Ye and J. Zhang, "Electromagnetically induced transparency-like effect in the degenerate triple-resonant optical parametric amplifier," Opt. Lett. **33**, 1911–1913 (2008).
26. J. Sun, Z. Zuo, X. Mi, Z. Yu, Q. Jiang, Y. Wang, L.-A. Wu, and P. Fu, "Two-photon resonant four-wave mixing in a dressed atomic system," Phys. Rev. A **70**, 053820 (2004).
27. J. Wang, L. Kong, X. Tu, K. Jiang, K. Li, H. Xiong, Y. Zhu, and M. Zhan, "Electromagnetically induced transparency in multi-level cascade scheme of cold rubidium atoms," Phys. Lett. A **328**, 437–443 (2004).
28. M. Xiao, L.-A. Wu, and H. J. Kimble, "Precision measurement beyond the shot-noise limit," Phys. Rev. Lett. **59**, 278–281 (1987).
29. M. Xiao, L.-A. Wu, and H. J. Kimble, "Detection of amplitude modulation with squeezed light for sensitivity beyond the shot-noise limit," Opt. Lett. **13**, 476–478 (1988).
30. D. F. Walls, "Squeezed states of light," Nature **306**, 141–146 (1983).
31. E. Arthurs and M. S. Goodman, "Quantum correlations: a generalized Heisenberg uncertainty relation," Phys. Rev. Lett. **60**, 2447–2449 (1988).